Flux penetration of an HTS coated-conductor tape by an approaching permanent magnet

R. W. Taylor[a,b,*], T. Booth[a,b], M. D. Ainslie[c], H. W. Weijers[a], R. A. Badcock[a] and C. W. Bumby[a,b]

[a]*Paihau-Robinson Research Institute, Victoria University of Wellington, Lower Hutt, 5010, New Zealand*
[b]*MacDiarmid Institute, Victoria University of Wellington, Wellington, 6140, New Zealand*
[c]*Department of Engineering, King's College London, London, WC2R 2LS, United Kingdom*

ABSTRACT

Interactions between inhomogeneous magnetic fields and a superconductor lie at the heart of several high-temperature superconducting (HTS) devices. An example is the situation where the magnetic field from a small permanent magnet (PM) is applied to a coated-conductor HTS tape, such that flux penetrates the superconductor. The PM field is highly spatially inhomogeneous, such that there is significant variation in the applied field magnitude and direction across the tape. This leads to a varying local critical current density, $J_c(B, \theta)$, across the tape, and consequently different 'shielding' (magnetic flux penetration) behaviour than is the case for a uniform applied field. Here, we report results from measurements and numerical simulations of the penetrating magnetic field within an HTS coated-conductor tape which occur as a PM dipole approaches from a distance. Electromagnetic simulations were performed using a finite-element model based on the **H**-formulation, and which incorporated experimentally-measured anisotropic $J_c(B, \theta)$ properties from a coated-conductor tape. This showed good agreement with experimental measurements. The effects of varying key modelling assumptions and parameters were then studied, including changing the widths of the PM and HTS tape and the magnitude of $J_c(B, \theta)$.

The inhomogeneity of the PM field leads to a characteristic gull-wing distribution of magnetic flux across the superconductor at elevated applied fields. Close approach of the PM to the tape suppresses J_c in the centre of the tape, and this results in the observation of a characteristic maxima for the total shielding currents circulating in the tape. A figure of merit is introduced which uses this effect to provide a threshold definition for 'full flux penetration' of an HTS tape by an inhomogeneous dipole field.

1. Introduction

The interactions between a permanent magnet (PM) and a superconductor are integral to several types of high-temperature superconducting (HTS) devices. The applied field from a PM is typically highly spatially inhomogeneous, with flux concentrated at the centre of each pole face and large field gradients occurring near its edges. As the basis for levitation applications, where strong magnetic field gradients occur perpendicular to the thrust direction [1], the PM-bulk superconductor interaction has been studied in great detail [2–7]. However, there have been relatively few detailed studies of the interactions between an inhomogeneous applied magnetic field of a PM and a thin HTS coated-conductor tape [8–11].

Recent detailed studies of the interaction between an HTS tape and a PM narrower than the tape width have been motivated by advances in understanding the HTS dynamo device [12–15]. In that device, a narrow PM traverses a coated-conductor with a flux gap of the order of a few millimetres [16]. When connected to a circuit, HTS dynamos produce a time-averaged DC voltage and can be used to inject current into a superconducting coil [17]. An interesting feature of experimental HTS dynamos is that there is a maximum flux gap between the PM and tape beyond which the device no longer exhibits a measurable output [10, 11]. This corresponds to the flux gap beyond which shielding currents in the tape prevent the applied flux from fully penetrating the tape. In an HTS dynamo, the lateral motion of the PM across the tape complicates matters, as the locally-induced emf causes overcritical eddy currents ($J > J_c$) to also flow within the tape [13]. As a result, this situation does not directly correspond to the quasi-static flux penetration limit of the tape.

Analytical critical-state models of the behaviour of superconducting strips, such as the Brandt model [18–21], provide useful tools to describe the behaviour of HTS tapes in the presence of uniform applied magnetic fields. However, key underlying assumptions of these models (the Bean limit, $n \to \infty$; and J_c = constant) are not generally experimentally valid. For example at liquid nitrogen temperatures (77 K), commercially available HTS tapes exhibit typical n-values between 20 and 40 [22] and thus are not well-described by the Bean limit. Even at 4.2 K, the n-values of many commercial tapes do not exceed 60 [23]. Common analytical models also assume a constant critical current density, J_c, but real HTS tapes are affected by the local applied field such that the critical current has a magnetic field-angular dependence, $J_c(B, \theta)$ [22]. Predicting flux penetration behaviour in this case requires a numerical model that has been validated by experimental data.

---

*Corresponding author

✉ ross.taylor@vuw.ac.nz (R.W. Taylor)

ORCID(s): 0000-0001-7497-6442 (R.W. Taylor); 0000-0003-0466-3680 (M.D. Ainslie); 0000-0002-6630-5048 (H.W. Weijers); 0000-0003-0219-9570 (R.A. Badcock); 0000-0001-8555-2469 (C.W. Bumby)

In this work, a numerical finite-element (FE) model has been constructed to capture the magnetic field and current behaviour of real coated-conductor tapes during the quasi-static approach of a PM dipole, which applies an inhomogeneous perpendicular applied field component to the tape. This has been constructed using the commercial FE modelling software COMSOL Multiphysics®. The FE model utilises n-values and $J_c(B, \theta)$ data extracted from experimental measurements of real coated-conductor tapes. Results from the FE model are then compared to experimental data, validating the qualitative features of the model and providing useful insights into the physical origin of the experimental observations. This work also compares computed results from a 'constant J_c' FE model, as this is a commonly used simplifying assumption when modelling HTS tapes. The effects of changing the relative size parameters of the PM and HTS tape are also examined, as these impact on shielding behaviour and are of interest in the context of the HTS dynamo [24, 25].

2. Modelling Methodology

The geometry of the inhomogeneous PM model is shown in Figure 1a, with the 2D case (infinitely long in the z-direction) assumed for simplicity. A PM of remanent flux density $||B_r|| = 1.5$ T, corresponding to a strong N52 grade PM, is centred at a flux gap d beneath an HTS coated-conductor tape, such that the axis of the PM is perpendicular to the wide face of the tape.

A segregated **H**-formulation FE model as used in [6, 26] was employed. This comprises a magnetostatic PM model and a time-dependent **H**-formulation [27, 28] model of the HTS tape. The two models are coupled along the outer boundaries of the **H**-formulation domain by summing the applied field from the PM, $\mathbf{H}_{ext}$, and the self-field of the tape, $\mathbf{H}_{self}$, caused by flow of the induced currents within the tape. Variation of the flux gap is implemented by applying a translation operator to $\mathbf{H}_{ext}$. At each time step, the 2D Biot-Savart law is integrated numerically over the HTS tape
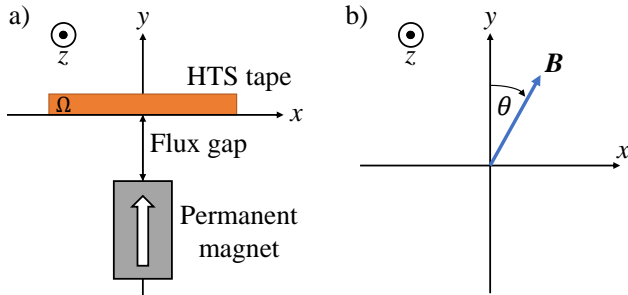

Figure 1: a) Geometry of the inhomogeneous applied field model. A permanent magnet is centred under an HTS tape, and the flux gap between them is reduced. b) Definition of θ using the same axes.

Figure 2: Example of logarithmic meshing in the tape sub-domain to enhance definition at the centre and edges. The thickness of the tape is artificially expanded in the vertical direction for visualisation purposes.

subdomain, Ω, to calculate $\mathbf{H}_{self}$:

$$H_{\text{self},x}(x, y, t) = \frac{1}{2\pi} \iint_\Omega \frac{-J_z(x', y', t) \cdot (y - y')}{(x - x')^2 + (y - y')^2} dx' dy', \quad (1)$$

$$H_{\text{self},y}(x, y, t) = \frac{1}{2\pi} \iint_\Omega \frac{J_z(x', y', t) \cdot (x - x')}{(x - x')^2 + (y - y')^2} dx' dy'. \quad (2)$$

The behaviour of the tape is dependent on the ramp rate of the applied homogeneous field/approach speed of the PM. For consistency and to reduce time-dependent effects, a slow ramp rate of 5 mTs^{-1} and magnet approach speed of 0.5 mms^{-1} was used throughout.

The non-linear behaviour of the HTS material is captured using the E-J power law [29–31]

$$\mathbf{E} = \frac{E_0}{J_c} \left| \frac{J}{J_c} \right|^{n-1} \mathbf{J}, \quad (3)$$

where $E_0 = 1$ µV/cm and $\mathbf{E} = \rho\mathbf{J}$. The other equations that govern the model are Faraday's and Ampère's laws, solving for the independent variables, the magnetic field strength $\mathbf{H} = [H_x, H_y]$.

To avoid the logarithmic singularity that occurs when modelling superconductors in 2D [18] and thus improve convergence, the superconducting layer of the HTS tape was modelled with a thickness of 10 µm, as opposed to its actual thickness of 1.3 µm. This approximation has been used previously under both homogeneous [32] and inhomogeneous [12, 13, 26] applied fields, and the accuracy of this assumption was confirmed through comparison with limited simulations using a thickness of 1.3 µm. The HTS subdomain was meshed using two logarithmic meshes meeting at the centre of the tape to give greater resolution at the tape centre and edges, as shown in Figure 2.

The numerical model employed experimentally-measured $I_c(B, \theta)$ data measured from two different HTS tapes using the SuperCurrent Facility in New Zealand [33]. These parameters were converted to equivalent critical current densities, corrected for self-field effects using the technique presented in [34] and input into the model via a two-variable, direct interpolation [35]. Figure 3 shows the measured $I_c(B, \theta)$ and $n(B, \theta)$ values at 77 K from a 12 mm wide copper-plated SuNAM SCN12700-210222-01 GdBCO tape, that was used in the experimental flux-penetration measurements. Figure 4 shows measured data for a SuperPower SF12050CF tape, which was used for other numerical modelling comparisons. For the SuperPower tape, a constant n-value of 20 was employed, which is a reasonable approximation for the measured values [12]. To enable full 360° angle-dependence
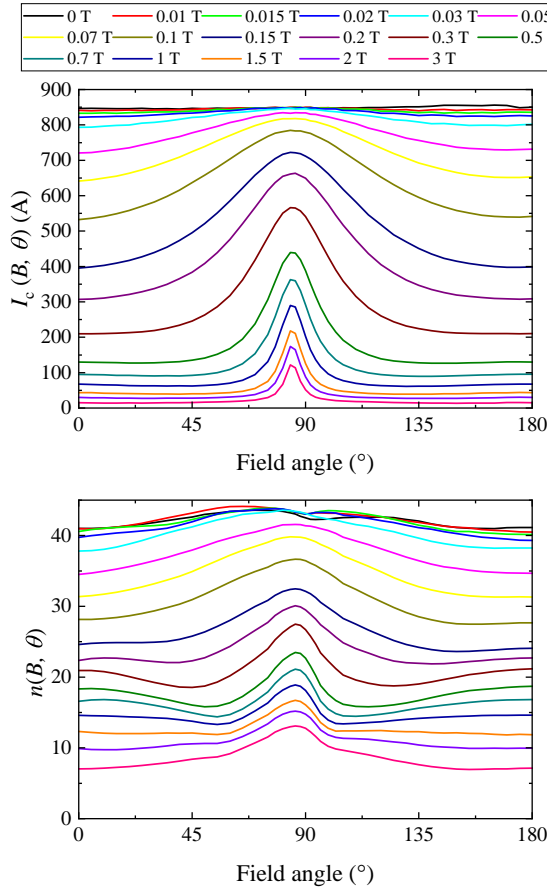
Figure 3: Experimental in-field $I_c(B, \theta)$ (top) and $n(B, \theta)$ (bottom) data of the 12 mm wide SuNAM SCN12700-210222-01 HTS tape used in this work. The data was measured at 77 K at the SuperCurrent facility [33], and is used, after correction for self-field effects using the technique presented in [34], as the input data for $J_c(B, \theta)$. Note that $\theta = 0°$ denotes field applied parallel to the tape and the $n(B, \theta)$ data has been smoothed using the Savitzky-Golay method.

of I_c to be utilised within the model, the data in each of these figures was mirrored around $\theta = 180°$.

The N42 grade PM used for experimental validation in this work had a specified remnant magnetisation of $||B_r|| = 1.3$ T at room temperature. However the performance of Nd-Fe-B magnets is temperature dependent, so the $||B_r||(T = 77$ K) value used in the model was taken to be 87% of the room temperature value, in accordance with the manufacturer's data [36].

In this work, numerical simulations have been performed to investigate and compare the significance of various parameters on the shielding behaviour of a tape. A useful parameter for these comparisons is the total absolute shielding currents flowing within the tape at any moment, which is defined herein as:

$$I'_z = \iint_\Omega |J_z| \cdot d\Omega, \tag{4}$$

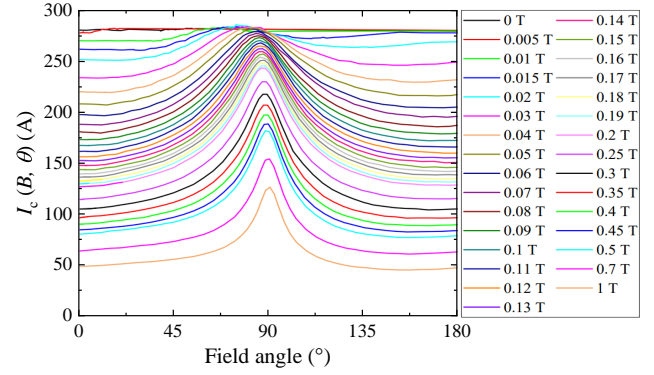where Ω denotes the cross-sectional area of the tape.

Figure 4: Experimental in-field $I_c(B, \theta)$ data of SuperPower SF12050CF HTS tape at 77.5 K in magnetic fields of up to 1 T measured at the SuperCurrent facility [33]. The data is used, after correction for self-field effects using the technique presented in [34], as the input data for $J_c(B, \theta)$.

3. Experimental Methodology

Experiments employed a scanning Hall probe arrangement in liquid nitrogen to measure the penetrating magnetic field profile behind a HTS tape (12 mm GdBCO tape, SuNAM SCN12700-210222-01). The apparatus is shown in Figure 5. A length of HTS tape was supported on a 0.5 mm thick aluminium shim atop three machined aluminium plinths, screwed into a non-conductive base. The displacement of a PM below the tape was varied by translating a supporting aluminium bar using nylon lead screws. A set of 1 mm thick glass composite (G10) spacers were used to define the flux gap between the tape and PM. The tape was connected to copper blocks at each end for mechanical stability, and the position of the middle plinth adjusted as necessary to ensure the physical centres of the magnet and tape were aligned.

An N42 grade Nd-Fe-B PM, of dimensions $6 \times 12 \times 12$ mm^3 and magnetised normal to two of its 6×12 mm^2 cross-sections, was used in the experiment to validate the model. In the experiment the south pole of the magnet was facing the bottom of the tape and the shortest dimension of the magnet was parallel to the width of the tape. The perpendicular magnetic field component near the top surface of the tape was measured using a P15A Hall-effect sensor (Advanced Hall Sensors Ltd), via an analogue-to-digital converter from National Instruments. This sensor was initially calibrated across a range of cryogenic temperatures and applied magnetic fields of up to 1 T using a Physical Property Measurement System from Quantum Design Inc.

The Hall sensor was attached to a boom that could be electromechanically translated along three orthogonal axes with an accuracy of 50 μm. Prior to the experiment, with the tape in the normal conducting state, the sensor was placed just in contact with the tape surface, and then raised 0.2 mm to ensure no contact with the tape at any later point in the procedure. The gap between the sensor and tape increased slightly as the apparatus was cooled due to
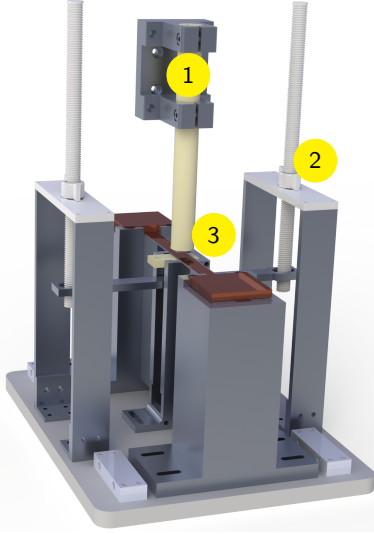
Figure 5: Apparatus used to measure penetrating field from a Nd-Fe-B permanent magnet applied to an HTS tape. (1) A Hall sensor is mounted on a movable boom. Nylon lead screws (2) are used to raise the magnet assembly (3) towards the tape.

thermal contraction of the plinths and insulating base. This contraction was not measured, but is estimated to be in the order of 1 mm.

To initialise each experimental run, the magnet was lowered as far as possible below the tape (approx. 90 mm), before the magnet, tape, and sensor were then immersed in liquid nitrogen. This closely approximated zero-field cooling of the tape. The magnet was then slowly raised until the aluminium support bar came into contact with the stack of G10 spacers. The perpendicular component of the magnet field was then measured at 0.2 mm steps across the width of the tape (above the centre-line of the magnet). Each field measurement comprised the mean of 1000 samples taken over 1 s. After each measurement profile across the tape was completed, a single spacer was removed and the process repeated at the next smallest flux gap. This continued until all spacers were removed.

To measure the applied field from the PM alone, similar measurements were undertaken under liquid nitrogen with the HTS tape removed.

4. Results and Discussion

4.1. Numerical modelling results for a uniform applied field

4.1.1. Homogeneous field applied under $J_c(B, \theta)$ assumption

Before exploring the interaction of a coated-conductor with a PM applied field, it is first important that the homogeneous (uniform) applied field case is well-understood. The calculated flux penetration and current density distribution

within a 12 mm wide SuperPower SF12050CF (I_c data shown in Figure 4) HTS tape is shown in Figure 6.

When a uniform magnetic field of magnitude B_{app} is applied perpendicular to the wide face of an HTS tape of width $2a$, flux penetrates the tape starting from the edges, as shown in Figure 6a. Shielding currents flow in each edge region whilst the central region remains flux free due to shielding effects [18, 37]. As B_{app} is increased, flux penetrates further into the tape (Figure 6b) until $B_{app} = B_{pen}$. This represents the minimum threshold applied field at which flux penetrates throughout, so that there is no longer a shielded region within the tape where $B = 0$ T [38]. At B_{pen} the tape is saturated with shielding currents such that $J(x, y) = J_c$ at all points, except for a narrow, finite current reversal region in the centre of the tape, Figure 6d. As B_{app} is increased further above B_{pen}, the field profile across the tape flattens, and the current reversal region narrows (Figure 6e-f).

4.1.2. Comparison of $J_c(B, \theta)$ vs. constant J_c assumption

The suppression of $J_c(B, \theta)$ at higher applied fields directly affects the total shielding currents flowing within the superconductor. This is illustrated in Figure 7, which shows the variation of I'_z (defined in Eq. 4) with increasing applied field. We see that for the $J_c(B, \theta)$ model (red line), I'_z initially increases with B_{app} as current extends deeper into the superconductor. However, a maximum in I'_z exists at $B_{app} = 27$ mT. We denote the position of this maxima as

$$B_{\max(I'_z)} = \mathrm{argmax}_{B_{app}}(I'_z). \tag{5}$$

At applied fields $< B_{\max(I'_z)}$, any increase in B_{app} causes a narrowing of the current reversal region and hence an overall increase in I'_z. However once $B_{app} > B_{\max(I'_z)}$, the suppression of $J_c(B, \theta)$ by the increased applied field now causes a greater reduction in I'_z than can be gained by further narrowing of the current reversal region. Comparison with the measured transport $I_c(B, \theta)$ behaviour of the tape (dotted green line) shows that I'_z follows the same declining trend for $B_{app} > B_{\max(I'_z)}$. Note that I'_z is always slightly less than I_c throughout the region plotted, because a finite n-value means there is always a small finite current reversal zone wherein $|J_z| < J_c$. The field profile and current distribution corresponding to $B_{\max(I'_z)}$ are shown in Figure 6c.

For the purposes of comparison, Figure 7 also shows the evolution of I'_z for a tape with a constant I_{c0} of 283 A (the self-field value of the I_{c0} data). In this case an idealised n-value of 120 has been used to closely approximate the Bean critical state model [39, 40]. It is notable that in this case (black line) no maximum is observed and instead I'_z asymptotically approaches I_{c0}. The maximum in I'_z in the field-dependent model occurs near the crossing point of the lines denoting I'_z for the constant-J_c model and $I_c(B, \theta)$, as this is approximately where the decrease in I'_z caused by field suppression of $I_c(B, \theta)$ outweighs the increase in I'_z from current filling.
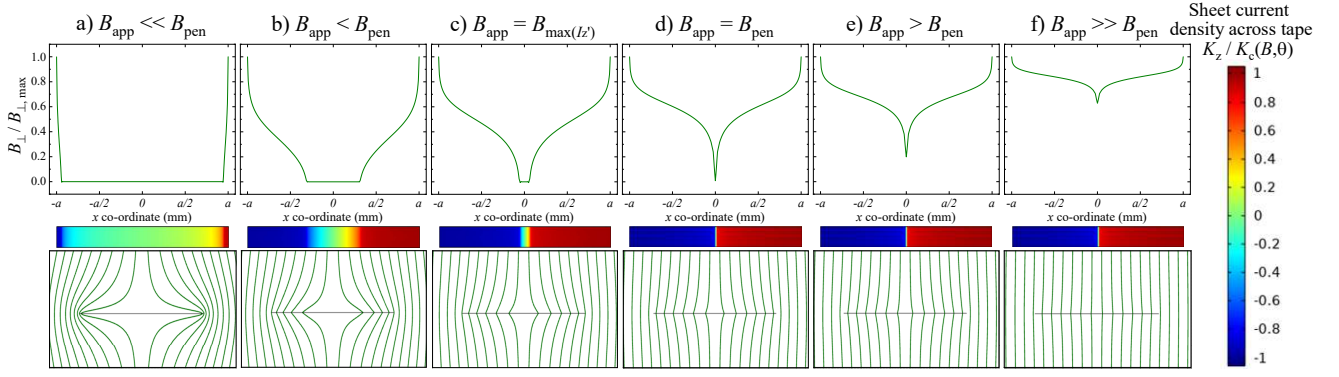
Figure 6: Homogeneous applied field case: Plots showing normalised magnetic flux density averaged over the thickness of the tape and sheet current density across an HTS tape assuming measured $J_c(B, \theta)$ dependence when a homogeneous field is applied perpendicular to the tape with magnitude B_{app}. (a) $B_{app} \ll B_{pen}$; (b) $B_{app} < B_{pen}$; (c) $B_{app} \lesssim B_{pen}$; (d) $B_{app} = B_{pen}$; (e) $B_{app} > B_{pen}$; (f) $B_{app} \gg B_{pen}$. Flux line plots (contours of constant **A**) are shown for each of these applied fields to illustrate shielding effects within the tape. The thickness of the tape is artificially expanded in the current plots for visualisation purposes.
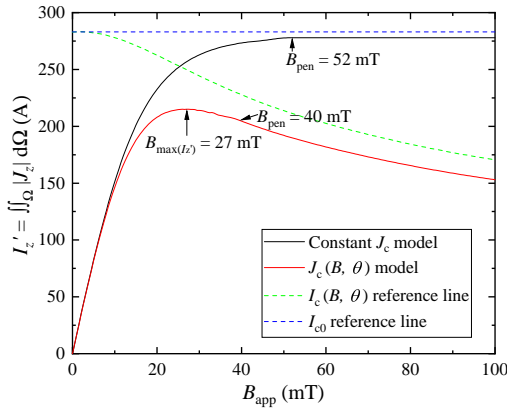

Figure 7: Applied field dependence of I'_z in a 12 mm × 10 μm HTS tape, for both angular field-dependent ($J_c(B, \theta)$) and independent (J_c = constant) critical current density assumptions. The homogeneous applied field is increased from 0 T to 0.1 T at a rate of 0.5 mTs^{-1}.

The fact that the maximum in I'_z is only observed when $J_c(B, \theta)$ suppression of a real HTS tape is considered, means that this effect cannot be reproduced by analytical (or numerical) models that assume a constant J_c. It is instructive to note that at $B_{\max(I'_z)}$, flux has not fully penetrated the tape. This means that the shielding currents flowing in a real tape (and the corresponding shielding field) reach a maximum value at an applied field which is significantly lower than that required for full flux-penetration of the tape, i.e. $B_{\max(I'_z)} < B_{pen}$.

4.2. Numerical modelling results for a PM dipole applied field

4.2.1. Inhomogeneous field applied under $J_c(B, \theta)$ assumption

The FE model described in Sec. 2 is now used to examine the flux penetration behaviour arising from the inhomogeneous applied field profile imposed by a PM dipole. As

above, shielding currents and penetrating flux are calculated for a 12 mm × 10 μm HTS tape assuming the $I_c(B, \theta)$ data from Figure 4 and $n = 20$. The flux gap between the tape and a 6 mm wide and 12 mm thick PM was gradually reduced from 50 mm to 0.5 mm at a rate of 0.5 mms^{-1}.

The applied field from a PM is concentrated at the centre of each pole face, and diverges with increasing distance from the PM. This is readily seen in the flux line plot shown in Figure 8f where the PM lies within the plotted field of view. However, at large axial displacements the field gradients are low. In this case the applied field approximates to the homogeneous applied field case, and shielding currents flow to prevent flux from penetrating the central region of the tape, as shown in Figure 8a. As the flux gap between the PM and tape decreases, the applied perpendicular field increases, and flux penetrates progressively further into the tape, see Figure 8b and c. By this point the inhomogeneity of the field applied by the PM across the tape has become increasingly apparent, with the perpendicular component of the applied field at the centre of the tape now significantly higher than at either edge. Eventually flux penetrates throughout the tape such that there is no shielded region, at a threshold flux gap denoted here as $d = d_{pen}$. (This situation is analogous to B_{pen} for the uniform applied field). At $d = d_{pen}$ (Figure 8d), the tape is saturated with critical currents flowing throughout except for a small current-reversal region. Close examination reveals that this current-reversal region is located slightly off-centre in the tape due to the minor asymmetry observed in the $I_c(B, \theta)$ data for the SuperPower tape used in this simulation.

Significant differences to the homogeneous case are observed in the fully flux-penetrated region where $d < d_{pen}$. Most notably, the profile of the perpendicular field across the tape for $d < d_{pen}$ exhibits a gull-wing shape, with the field at the tape edges dropping below the field at the centre, due to the lower applied perpendicular field component at locations away from the PM centre line. This contrasting behaviour is
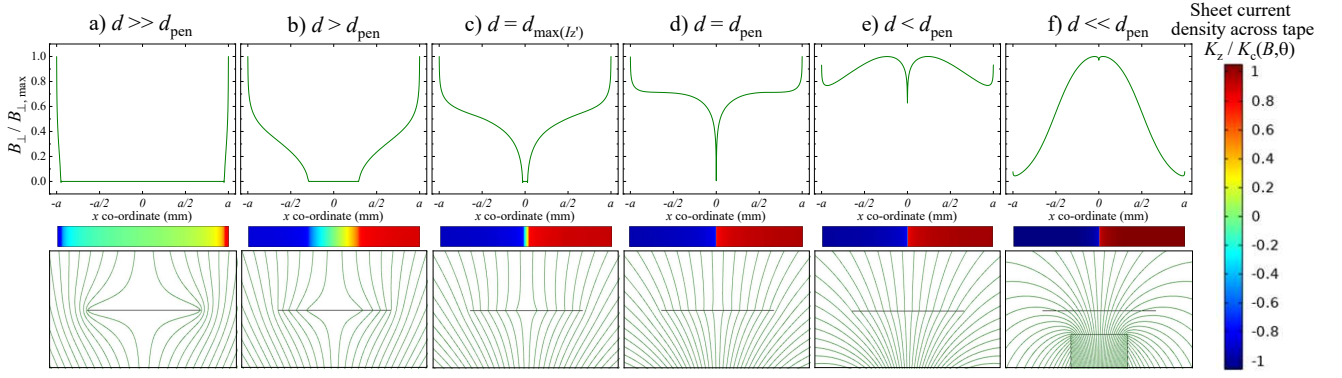
Figure 8: Inhomogeneous applied field case (PM dipole): Plots showing normalised magnetic flux density averaged over the thickness of the tape and sheet current density across an HTS tape assuming measured $J_c(B, \theta)$ dependence when a PM is situated at a flux gap, d. (a) $d \gg d_{pen}$; (b) $d > d_{pen}$; (c) $d \gtrsim d_{pen}$; (d) $d = d_{pen}$; (e) $d < d_{pen}$; (f) $d \ll d_{pen}$. Flux line plots (contours of constant $\mathbf{A}$) are shown for each of these gaps to illustrate shielding effects within the tape, and the inhomogeneity of the PM field. The thickness of the tape is artificially expanded in the current plots for visualisation purposes.

most clearly apparent when comparing the flux contours in FIGS. 6e and 8e.

4.2.2. Comparison of $J_c(B, \theta)$ vs. constant J_c assumption for inhomogeneous applied PM field

As in the homogeneous applied field case, shielding currents in the $J_c(B, \theta)$ model are suppressed at higher applied field magnitudes. This is illustrated in Figure 9.

Initially, as the PM approaches the superconductor from a distance, I'_z (red line) increases due to shielding currents extending further into the tape. A maximum is reached at $d = 19.0$ mm. We denote the position of this maxima as

$$d_{\max(I'_z)} = \operatorname{argmax}_d \iint_\Omega |J_z| \cdot d\Omega. \tag{6}$$

Further decreasing d to $< d_{\max(I'_z)}$ leads to suppression of $I_c(B, \theta)$ (dotted green line) which outweighs the increase in shielding currents from further narrowing of the current reversal region. This situation is analogous to that observed in the uniform field, and in this case occurs at a similar maximum applied central field (28 mT versus 27 mT). Similarly, we also observe that the maximum shielding currents flow at a flux gap which is significantly larger than required for full flux penetration to the centre of the tape, i.e. $d_{\max(I'_z)} > d_{pen}$.

As before, Figure 9 also shows I'_z for a tape with constant I_{c0} of 283 A (the self-field I_c of the $I_c(B, \theta)$ data) and $n = 150$. For this case there is no maximum observed and instead I'_z increases with decreasing d to asymptotically approach I_{c0}. Field suppression of J_c throughout the tape also means that the penetration gap, d_{pen}, is smaller for the constant-J_c model than for the $J_c(B, \theta)$ model (12.2 mm vs. 13.5 mm).

4.3. Experimental Validation of Permanent Magnet Applied Field Model

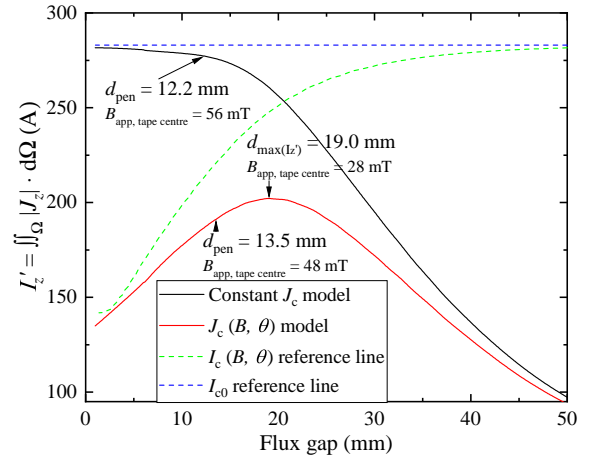To validate the model, the simulated results are compared to measured values from the experiment described in

Figure 9: Variation of I'_z in a 12 mm × 10 μm HTS tape as a 6 mm × 12 mm N52 grade PM is moved from a flux gap of 50 mm to a flux gap of 0.5 mm at a rate of 0.5 mms⁻¹. The model was run with a field dependent $J_c(B, \theta)$ using data from Figure 4 with $n = 20$, and again with a constant J_c corresponding to I_{c0} of the same tape with $n = 150$.

Sec. 3. The field measured experimentally by the Hall probe, B_{TOT}, is the y-component of the penetrating field behind the tape, and can be expressed as the sum of the y-components of the PM field, B_{PM}, and the field due to screening currents flowing in the HTS tape, B_{HTS}:

$$B_{TOT} = B_{PM} + B_{HTS}. \tag{7}$$

The coercive field of Nd-Fe-B is much greater than any shielding fields induced in this experiment [41], hence it is assumed that B_{PM} is constant and does not vary with B_{HTS}.

Figure 10 shows the experimentally measured field profiles (B_{TOT}) across the HTS tape, for a range of flux gaps between the PM and tape. Profiles computed from the FE model are also shown for comparison and show generally
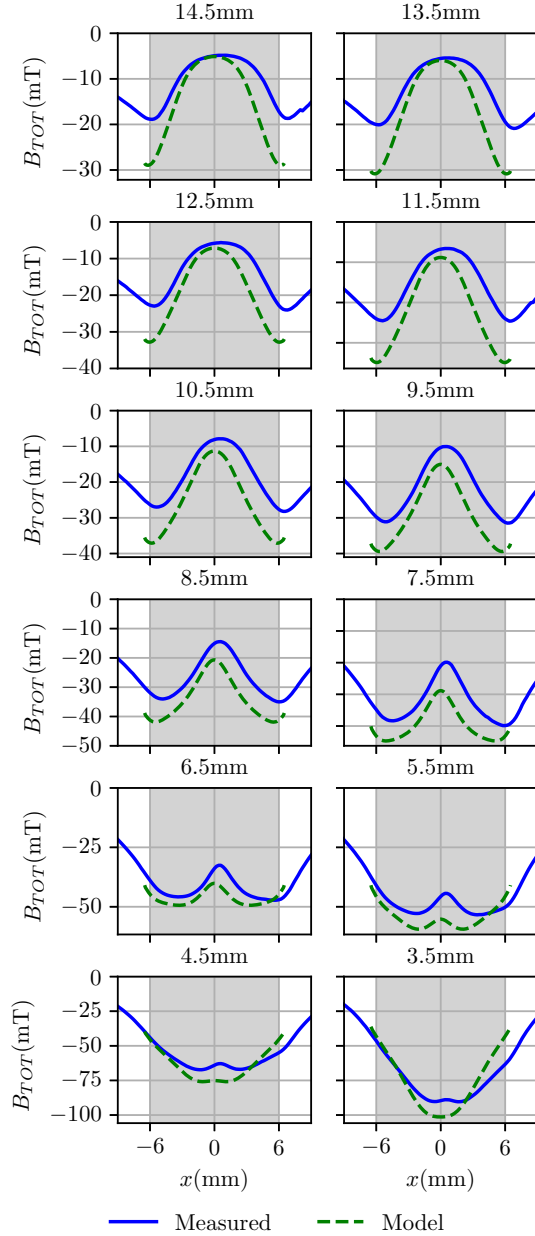
Figure 10: Experimentally measured field profiles behind the 12 mm coated-conductor tape (B_{TOT}) for a range of flux gaps, d, from 3.5 mm to 14.5 mm. Also shown for comparison are profiles computed from the FE model. The grey shaded area denotes the extent of the 12 mm wide tape. In particular, note the gull-wing profile within the tape that is most marked between $d = 4.5$ mm and $d = 8.5$ mm.

good agreement. In particular, note the characteristic gull-wing shape to the field profile within the boundaries of the tape (grey shaded region) that is particularly noticeable for flux gaps from about 5.5 mm to 8.5 mm. This clearly shows the magnitude of the penetrating field reaching a local maximum at the centre of the tape (rather than falling off monotonically from the edge as expected for a uniform applied field). The gull-wing appears upside-down here

compared to Figure 8, because the opposite magnet pole was positioned closest to the tape experimentally, making the observed fields negative.

The gull-wing profile is not visible in either the field of the PM alone or the field of the tape alone, but is rather due to the superposition of B_{HTS} and B_{PM}.

Furthermore, the gull-wing profile cannot occur unless the applied field is inhomogeneous; the tape characteristics alone do not account for it. To understand why this is so, consider just the left half of the tape and the component of current that is in the z-direction. By Ampère's law this is $(\nabla \times \mathbf{B})_z = \mu_0 J_z = \partial B_y / \partial x - \partial B_x / \partial y$ (displacement current is neglected). B_y is the perpendicular component of the field (corresponding to B_{TOT} above). The gull-wing implies that as we move from the left edge towards the centre, $\partial B_y / \partial x$ is at first negative, then positive. But the shielding current J_z is only positive throughout this domain (as is confirmed by the FE model). Therefore, $\partial B_x / \partial y$ must be negative, and its magnitude must be relatively large when $\partial B_y / \partial x$ is most negative. This behaviour is due to the divergent curvature of the applied inhomogeneous field. The field becomes more parallel moving towards the edges of the tape, and the curvature is sufficient to outweigh the simultaneous weakening of the field with distance from the centre of the magnet.

While the shape of the field profile is consistent between model and experiment, the absolute magnitudes are slightly higher in the model than in the experiment. This is attributed to experimental uncertainties including: absolute measurement error of the flux gap; parallelism of magnet, tape, and sensor; and the exact cryogenic magnetisation of the full permanent magnet. Another factor that may contribute to this effect is that in order to reduce the model to 2D, the magnet is assumed infinite in the z-direction. In reality the magnet is finite, and field divergence at the point of measurement will cause the measured value to be lower than that calculated in the model.

Although the total current within the HTS tape, I'_z, cannot be measured directly in the experiment, the field due to the shielding currents flowing in the HTS tape, B_{HTS}, can be calculated from Eq. 7. This is a dipole field with a central peak. Figure 11 shows the evolution of this peak shielding field, $\max_x(B_{\text{HTS}})$, as a function of flux gap. Both experimental measurements and the FE model show that this peak shielding field initially increases as the flux gap decreases, but eventually reaches a maximum value beyond which it then declines. This occurs because initially critical currents gradually 'fill up' the tape from the edges inwards, shielding the inner regions of the tape from flux until the tape is fully saturated. However, as the magnet gets closer, the incident field magnitude becomes large, which results in $J_c(B, \theta)$ suppression. This reduces the total shielding currents flowing in the tape, and hence reduces the peak shielding field. The highest value of $\max_x(B_{\text{HTS}})$ occurs at a flux gap of (7.5 ± 1) mm in both the experiment and the model.
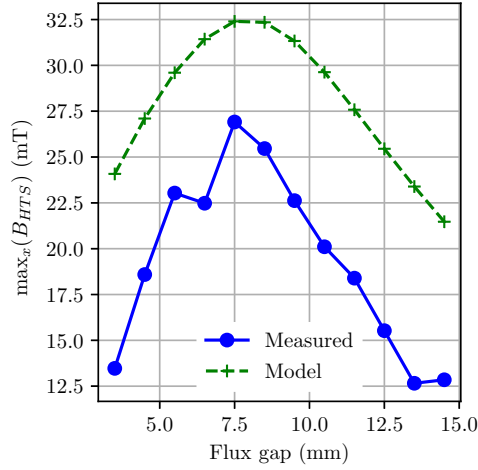
Figure 11: Maximum B_{HTS} by flux gap. This corresponds to the absolute currents flowing in the tape. Note that currents reach a maximum well before the magnet reaches the tape.

4.4. Critical Comparison of Common Modelling Assumptions

This section discusses the advantages and disadvantages of different modelling assumptions, and summarises key points mentioned in the previous sections.

4.4.1. Modelling using $J_c(B, \theta)$ vs. a constant J_c assumption

A constant J_c is commonly assumed to reduce simulation time. The inhomogeneous PM approach model described in this work, with the parameters used in Sec. 4.2.2, took 54 min to run with a constant J_c, and 56 min when using experimentally measured data. This difference is slight, however could become significant in a system of many tapes and/or multiple PM arrays.

Another reason for this assumption is that $I_c(B, \theta)$ data can be difficult to measure, leading to limited access, particularly at temperatures other than 77 K. This makes it difficult to incorporate realistic tape behaviour at the lower temperatures more appropriate for real engineering applications. An online repository containing $I_c(B, \theta)$ data with temperature dependence for numerous commercial HTS tapes can be found here [42].

There are numerous disadvantages to assuming that J_c is constant. Sections 4.1.2 and 4.2.2 describe the flow of shielding currents within the tape for homogeneous and inhomogeneous applied fields respectively, and in each case significant differences were observed between models with constant J_c and $J_c(B, \theta)$ dependence. It is important that the effects of J_c suppression are considered in context when designing models. For example, consider Figure 9. If a device requires the largest possible shielding current, the constant J_c data implies that as small a flux gap as possible is desirable, however experimentally this would lead to almost half of the expected current due to suppression effects.

Assuming that J_c is constant also ignores any asymmetry that occurs within the tape. In the $J_c(B, \theta)$ case the electrical centre was found to be marginally off-centre, but this does not occur when J_c is assumed constant. There is little asymmetry in the $I_c(B, \theta)$ data of the tapes considered here, however significant asymmetry is possible, for example in SuperPower's Advanced Pinning tape.

4.4.2. Infinite, constant or field-dependent n-values

It is common to assume the Bean limit ($n \to \infty$), within which the current reversal zone is infinitesimally small [39, 40]. However, real superconductors have finite current reversal zones, which become narrower as the applied field is increased in magnitude. The current density over this region is continuous, and therefore in this region $|J| < J_c$, which reduces the total current capacity of the tape by an amount dependent on n. To investigate the significance of this n-dependent current limiting without interplay from field inhomogeneity effects, the constant J_c model under a homogeneous applied field from Sec. 4.1.2 was repeated with $n = 20$, 120 and 150. For $n = 20$, I_z', which quantifies the current carrying capacity, only reached 89.7% of I_c. As n was increased, the current reversal region at saturation became narrower, leading to I_z' values of 98.2% and 98.5% of I_c for $n = 120$ and 150 respectively. This shows that assumption of the Bean limit can significantly overestimate the current carrying capacity of HTS tapes.

The extent to which the field-dependence of n affects current carrying properties of tapes is considered by comparing results of the model from Sec. 3 when using the angular field-dependent $n(B, \theta)$ data from Figure 3 with results when using constant values of n. A constant value of $n = 20$ was considered, as this is commonly used in modelling, and $n = 35$ was also chosen, corresponding to the n-value measured for the tape under an applied field equal to that exhibited at the tape position when the PM is halfway through movement. There is little qualitative difference in I_z' as a function of flux gap for these values, as the tape saturates at large flux gaps, and the maximum of I_z' occurs at the same position to an accuracy of 0.1 mm for each n-value considered. The magnitude of the peak differs however, corresponding to the differences in current reversal region size. When $n = 35$, $\max(I_Z')$ is < 1% below the value for field-dependent n, and even when $n = 20$ this only extends to an $\approx 3\%$ difference.

4.4.3. Homogeneous vs. Inhomogeneous Applied Fields

To compare the homogeneous model results from Section 4.1.1 with the inhomogeneous model results in Section 4.2.1, the applied field magnitude at the tape centre, $B_{app, t.c.}$, is determined at the threshold flux gaps in the PM approach model. In the homogeneous model, the threshold values are $B_{pen} = 52$ mT when J_c is assumed constant, and $B_{\max(I_z')} = 27$ mT and $B_{pen} = 40$ mT when suppression effects are included. In the inhomogeneous model, the corresponding values are $B_{app, t.c.} = 56$ mT, $B_{app, t.c.} = 28$ mT and

$B_{\text{app, t.c.}}$ = 48 mT respectively. For each figure of merit, a slightly higher field is calculated at the tape centre in the inhomogeneous model than is applied in the homogeneous model.

When the applied field is above the threshold values, significant differences emerge between the homogeneous and PM applied field cases. The inhomogeneity of the PM causes a gull-wing shape to appear in the field profile across the tape, which becomes more pronounced the closer the PM moves to the tape (and thus the larger the inhomogeneity of the applied magnetic field from the PM at the tape position). This differs to the homogeneous case, where the field profile becomes increasingly flat as the magnitude of the field is increased.

The extent to which inhomogeneity affects results depends on the context, and whether or not a simplifying assumption is valid should be considered for the desired application.

4.5. Extension Studies

4.5.1. Effects of changing tape width

To investigate the effects of tape width on the current and field distribution, the model was run using a 6 mm × 12 mm N52 grade PM and repeated for HTS tapes of widths 1 mm and increasing in 3 mm increments from 3 mm to 30 mm, using $J_{\text{c}}(B, \theta)$ data from Figure 4. Figure 12 shows how I_z' changes as the PM approaches the tape for each tape width considered.

For tape widths of less than 18 mm, the behaviour is as before, with the peak becoming sharper as the tape width increases. However as the tape becomes much wider than the PM a second maximum starts to form in I_z'. This occurs due to the inhomogeneity of the PM. The return path of flux lines from the PM start to pass through the tape, with the magnitude of the field strength in regions of opposite flux being much less than in the central outward flux region, see Figure 13. This leads to less suppression of $J_{\text{c}}(B, \theta)$ in
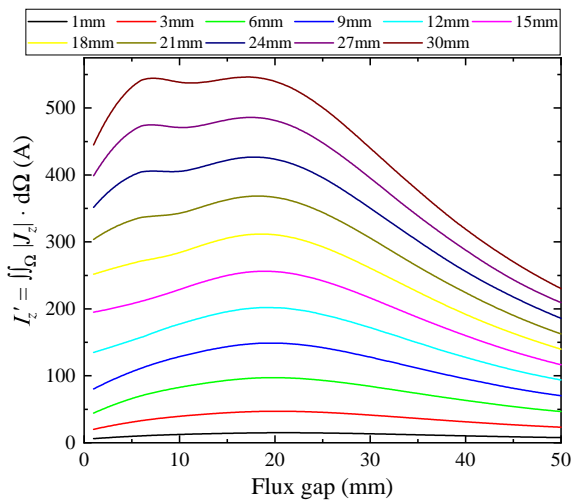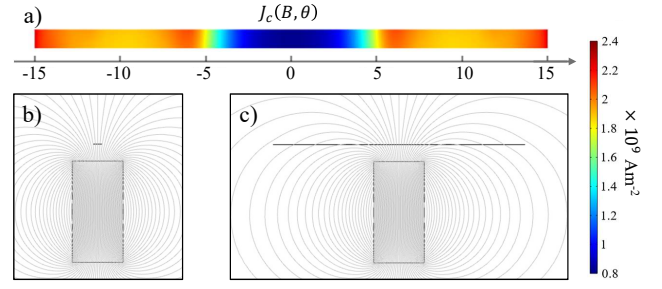

Figure 13: (a) $J_c(B, \theta)$ in a 30 mm × 10 µm HTS tape when a 6 mm × 12 mm N52 PM is at a flux gap of 2 mm away. The thickness of the tape is artificially expanded in the vertical direction for visualisation purposes. (b) and (c) show flux line plots (contours of constant **A**) for the system when a 6 mm × 12 mm N52 PM is at a flux gap of 2 mm from a 1 mm × 10 µm and 30 mm × 10 µm HTS tape respectively.
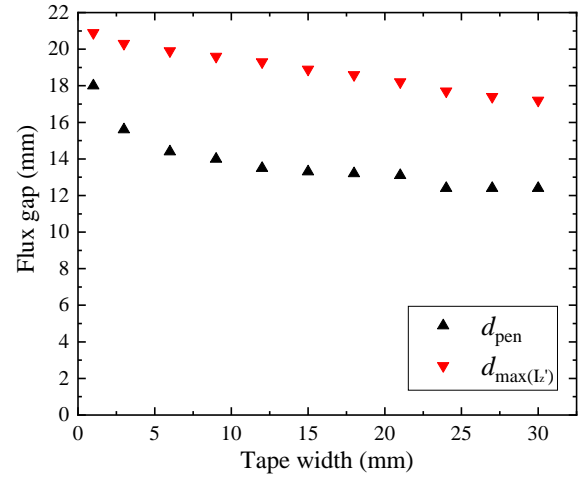

Figure 14: Flux gaps corresponding to the penetration threshold and maximum current flow for a range of tape widths (1-30 mm) and a 6 mm × 12 mm N52 PM.

these regions (see Figure 13a), allowing more current to flow within them and thus a higher I_z' is observed. As the PM moves closer to the tape, the field in these regions becomes stronger, suppressing I_c and causing I_z' to reduce again.

Figure 14 shows the values of the figures of merit for the different tape widths. For all widths, $d_{\max(I_z')}$ occurs at larger flux gaps than d_{pen}. As the tape width is increased, the flux gap at which the criteria is met reduces, as a stronger field is needed to suppress more tape. The decrease is not linear however, and flattens for tapes much wider than the PM.

4.5.2. Effects of changing PM width

The effects of PM width on the current and field distribution of a 12 mm × 10 µm HTS tape with $J_{\text{c}}(B, \theta)$ dependence were investigated by considering 12 mm long N52 grade PMs with widths of 2 mm and increasing in 3 mm increments from 3 mm to 30 mm, Figure 15 shows how I_z' changes as the PM approaches the tape.
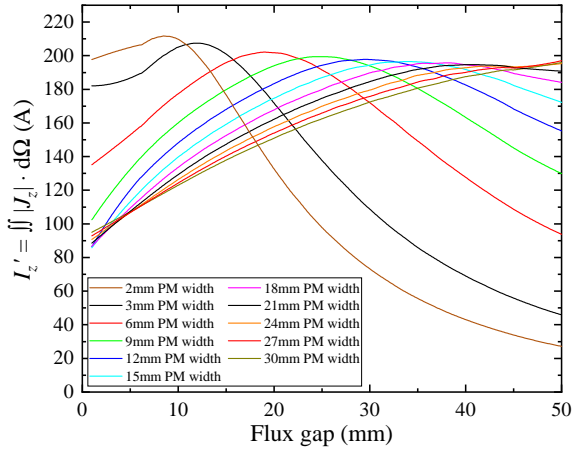

Figure 12: Variation of I_z' in a HTS tape as a function of flux gap for a range of tape widths (1-30 mm) with a 6 mm × 12 mm N52 PM.

Figure 15: Variation of I_z' in a 12 mm SuperPower SF12050CF HTS tape as a function of flux gap between the tape and a N52 PM of a range of widths (2-30 mm).
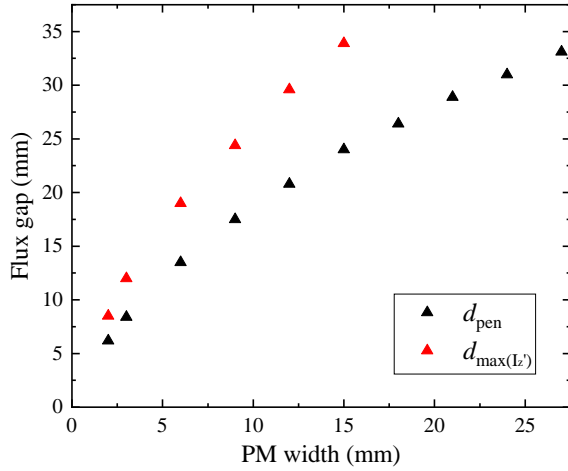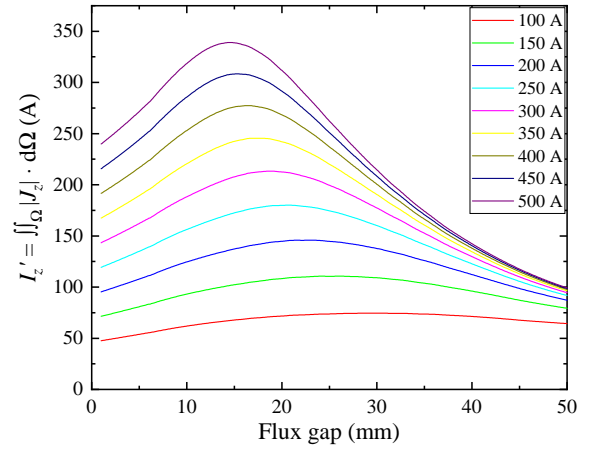

Figure 17: Variation of I_z' in a HTS tape as a function of flux gap between the tape and a 6 mm × 12 mm N52 grade PM. for a range of tape $I_c[s.f, 77\ \text{K}]$ (100-500 A).
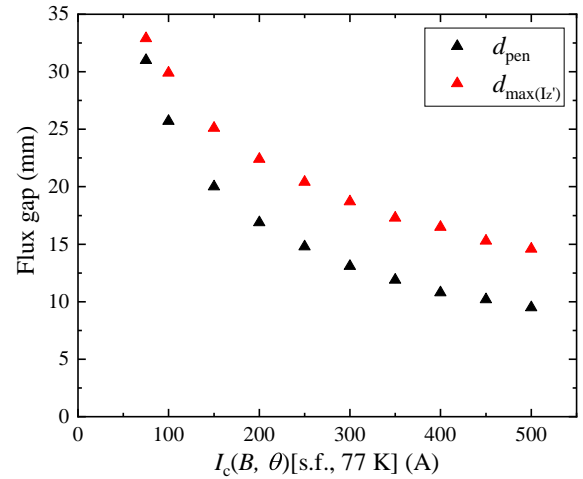

Figure 16: Penetration threshold and maximum current flux gaps as a function of PM width for a 12 mm SuperPower SF12050CF HTS tape.

Figure 18: Penetration threshold and maximum current flux gaps as a function of tape $I_c[s.f, 77\ \text{K}]$.

At large flux gaps, I_z' increases with PM width because the flux across the tape width increases with little suppression of the critical current. As the PM becomes much wider than the tape this effect is limited as the field across the tape position is more homogenised.

When the PM approaches the tape, peaks form in I_z' due to shielding currents flowing deeper within the tape, increasing I_z' until the suppression of $J_c(B,\theta)$ is sufficient to reduce I_z' again. As the PM width increases, the peaks have a lower maximum and become broader due to increased suppression across the width of the tape.

At small flux gaps, a narrower PM has a higher I_z' because $J_c(B,\theta)$ is only suppressed heavily at the centre due to the inhomogeneous field from the PM, as opposed to across the whole width for wider PMs.

Figure 16 shows the values of the figures of merit for different PM widths. For all widths, $d_{\max(I_Z')}$ occurs at larger flux gaps than d_{pen}. As the PM becomes wider, the flux gaps at which the criteria occur increase, however the rate is not constant, and begins to level off as the PM becomes wider, this is explained by the field from the PM becoming more homogeneous across the tape width.

4.5.3. Effect of Scaling I_c

The effects of scaling I_c by a multiplication factor were investigated by scaling the $I_c(B,\theta)$ data presented in Figure 4. Thus, we assume the same overall pinning characteristics, i.e. angular dependence, and scale the $I_c(B,\theta)$ data with respect to $I_c[s.f, 77\ \text{K}]$, from 100 A to 500 A in 50 A increments.

The I_z' curves are presented in Figure 17. As $I_c[s.f, 77\ \text{K}]$ is increased, the peaks become sharper, and occur at lower flux gaps because the increased current flow from the reduction of the current reversal region is more significant than suppression effects.

The figures of merit, presented in Figure 18, both occur at lower flux gaps as the critical current of the tape

is increased, because stronger shielding currents require a larger applied field to be overcome. The relationship between both figures of merit and $I_c[s.f, 77 \text{ K}]$ is non-linear, with a sharper drop off at lower critical currents.

5. Conclusion

In this work, a model based on the segregated **H**-formulation was constructed and experimentally validated to investigate the interactions between a HTS tape and the inhomogeneous magnetic field from a permanent magnet. The effects of changing key system parameters, including the PM and tape widths and critical current, were investigated.

Two figures of merit were introduced for both homogeneous (B_{pen} and $B_{\text{max}(I'_z)}$) and inhomogeneous (d_{pen} and $d_{\text{max}(I'_z)}$) applied fields. These were used to compare the effects of common modelling assumptions, and significant differences were observed in the field and current distributions within the tape when ignoring the field-dependence of J_c and inhomogeneity in the applied field from the magnet. When J_c is assumed constant, the shielding currents within a tape are strongest for the highest applied fields. However, in real HTS tapes, suppression of J_c at large applied fields limits shielding current flow within the tape, and a maximum is observed as the applied field is increased. For a 12 mm wide SuperPower SF12050CF HTS tape under a homogeneous applied field, simulations showed that shielding currents were strongest at the highest applied field considered ($B_{\text{app}} = 100 \text{ mT}$) when J_c was assumed constant, whereas shielding currents peaked at $B_{\text{app}} = 27 \text{ mT}$ when measured $J_c(B, \theta)$ data was used. Similarly in the case where an N52 grade PM approaches a 12 mm wide SuperPower SF12050CF HTS tape without a background field, shielding currents peaked when the magnet was as close to the tape as considered ($d = 0.5 \text{ mm}$) and at $d = 19 \text{ mm}$ for constant and field-dependent J_c assumptions respectively.

The flux penetration and current distribution of an HTS tape due to an approaching PM is explained, with a distinct gull-wing shape observed in the field profile across the tape due to the inhomogeneity of the applied field when the flux penetrates throughout the tape. This gull-wing does not form when the applied field is assumed homogeneous. As the inhomogeneity within the system increases, such as by moving the magnet closer or increasing the tape-to-magnet width ratio, the differences to the homogeneous case become more pronounced.

Experimental measurements broadly agree with predictions from the FE model. In particular, the gull-wing shape caused by the curvature of the magnetic field of the magnet was observed. Experimental observations also showed that the shielding currents flowing in the tape reach a maximum when the magnet is still relatively far away from the HTS tape, before subsequently declining as the flux gap is further reduced. In both the model and experiment, the measured field value corresponding to the maximum total shielding currents was observed when an N42 grade PM was at a flux gap of (7.5 ± 1) mm from a SuNAM SCN12700-210222-01 HTS tape.

Insights obtained from this work will inform the understanding and design of future HTS devices where permanent magnets interact with HTS tapes, such as HTS dynamo flux pumps.

References

[1] L. Schultz, O. de Haas, P. Verges, C. Beyer, S. Rohlig, H. Olsen, L. Kuhn, D. Berger, U. Noteboom, U. Funk, Superconductively levitated transport system - the SupraTrans project, IEEE Transactions on Applied Superconductivity 15 (2005) 2301–2305.

[2] C. Navau, N. Del-Valle, A. Sanchez, Macroscopic modeling of magnetization and levitation of hard type-II superconductors: The critical-state model, IEEE Transactions on Applied Superconductivity 23 (2013) 8201023.

[3] E. Perini, G. Giunchi, M. Geri, A. Morandi, Experimental and numerical investigation of the levitation force between bulk permanent magnet and MgB$_2$ disk, IEEE Transactions on Applied Superconductivity 19 (2009) 2124–2128.

[4] F. Sass, G. G. Sotelo, R. de Andrade Junior, F. Sirois, H-formulation for simulating levitation forces acting on HTS bulks and stacks of 2G coated conductors, Superconductor Science and Technology 28 (2015) 125012.

[5] A. Morandi, M. Fabbri, P. L. Ribani, A. Dennis, J. Durrell, Y. Shi, D. Cardwell, The measurement and modeling of the levitation force between single-grain YBCO bulk superconductors and permanent magnets, IEEE Transactions on Applied Superconductivity 28 (2018) 3601310.

[6] L. Quéval, K. Liu, W. Yang, V. M. R. Zermeño, G. Ma, Superconducting magnetic bearings simulation using an H-formulation finite element model, Superconductor Science and Technology 31 (2018) 084001.

[7] F. Grilli, A. Morandi, F. D. Silvestri, R. Brambilla, Dynamic modeling of levitation of a superconducting bulk by coupled H-magnetic field and arbitrary lagrangian–eulerian formulations, Superconductor Science and Technology 31 (2018) 125003.

[8] M. Zehetmayer, M. Eisterer, H. W. Weber, Simulation of the current dynamics in a superconductor induced by a small permanent magnet: application to the magnetoscan technique, Superconductor Science and Technology 19 (2006) S429–S437.

[9] M. Zehetmayer, R. Fuger, F. Hengstberger, M. Kitzmantel, M. Eisterer, H. Weber, Modified magnetoscan technique for assessing inhomogeneities in the current flow of coated conductors – theory and experiment, Physica C: Superconductivity and its Applications 460-462 (2007) 158–161.

[10] Z. Jiang, C. W. Bumby, R. A. Badcock, H.-J. Sung, N. J. Long, N. Amemiya, Impact of flux gap upon dynamic resistance of a rotating

HTS flux pump, Superconductor Science and Technology 28 (2015) 115008.

[11] A. Ghabeli, E. Pardo, Modeling of airgap influence on DC voltage generation in a dynamo-type flux pump, Superconductor Science and Technology 33 (2020) 035008.

[12] R. C. Mataira, M. D. Ainslie, R. A. Badcock, C. W. Bumby, Origin of the DC output voltage from a high-T_c superconducting dynamo, Applied Physics Letters 114 (2019) 162601.

[13] R. Mataira, M. Ainslie, A. Pantoja, R. Badcock, C. Bumby, Mechanism of the high-T_c superconducting dynamo: Models and experiment, Physical Review Applied 14 (2020) 024012.

[14] A. Ghabeli, E. Pardo, M. Kapolka, 3D modeling of a superconducting dynamo-type flux pump, Scientific Reports 11 (2021) 10296.

[15] L. Prigozhin, V. Sokolovsky, Two-dimensional model of a high-T_c superconducting dynamo, IEEE Transactions on Applied Superconductivity 31 (2021) 5201107.

[16] C. W. Bumby, Z. Jiang, J. G. Storey, A. E. Pantoja, R. A. Badcock, Anomalous open-circuit voltage from a high-T_c superconducting dynamo, Applied Physics Letters 108 (2016) 122601.

[17] C. Hoffmann, D. Pooke, A. D. Caplin, Flux pump for HTS magnets, IEEE Transactions on Applied Superconductivity 21 (2011) 1628–1631.

[18] E. H. Brandt, M. Indenbom, Type-II-superconductor strip with current in a perpendicular magnetic field, Physical Review B 48 (1993) 12893–12906.

[19] E. H. Brandt, Superconductors of finite thickness in a perpendicular magnetic field: Strips and slabs, Physical Review B 54 (1996) 4246–4264.

[20] G. P. Mikitik, E. H. Brandt, Critical state in thin anisotropic superconductors of arbitrary shape, Physical Review B 62 (2000) 6800–6811.

[21] G. P. Mikitik, E. H. Brandt, Generation of a dc voltage by an ac magnetic field in type-II superconductors, Physical Review B 64 (2001) 092502.

[22] X. Zhang, Z. Zhong, J. Geng, B. Shen, J. Ma, C. Li, H. Zhang, Q. Dong, T. Coombs, Study of critical current and n-values of 2G HTS tapes: Their magnetic field-angular dependence, Journal of Superconductivity and Novel Magnetism 31 (2018) 3847–3854.

[23] K. Tsuchiya, A. Kikuchi, A. Terashima, K. Norimoto, M. Uchida, M. Tawada, M. Masuzawa, N. Ohuchi, X. Wang, T. Takao, S. Fujita, Critical current measurement of commercial REBCO conductors at 4.2K, Cryogenics 85 (2017) 1–7.

[24] A. E. Pantoja, Z. Jiang, R. A. Badcock, C. W. Bumby, Impact of stator wire width on output of a dynamo-type HTS flux pump, IEEE Transactions on Applied Superconductivity 26 (2016) 4805208.

[25] R. Mataira, M. D. Ainslie, R. Badcock, C. W. Bumby, Modeling of stator versus magnet width effects in high-T_c superconducting dynamos, IEEE Transactions on Applied Superconductivity 30 (2020) 5204406.

[26] M. Ainslie, F. Grilli, L. Quéval, E. Pardo, F. Perez-Mendez, R. Mataira, A. Morandi, A. Ghabeli, C. Bumby, R. Brambilla, A new benchmark problem for electromagnetic modelling of superconductors: the high-T_c superconducting dynamo, Superconductor Science and Technology 33 (2020) 105009.

[27] B. Shen, F. Grilli, T. Coombs, Review of the AC loss computation for HTS using H formulation, Superconductor Science and Technology 33 (2020) 033002.

[28] B. Shen, F. Grilli, T. Coombs, Overview of H-formulation: A versatile tool for modeling electromagnetics in high-temperature superconductor applications, IEEE Access 8 (2020) 100403–100414.

[29] C. Plummer, J. Evetts, Dependence of the shape of the resistive transition on composite inhomogeneity in multifilamentary wires, IEEE Transactions on Magnetics 23 (1987) 1179–1182.

[30] J. Rhyner, Magnetic properties and AC-losses of superconductors with power law current—voltage characteristics, Physica C: Superconductivity 212 (1993) 292–300.

[31] E. H. Brandt, Susceptibility of superconductor disks and rings with and without flux creep, Physical Review B 55 (1997) 14513–14526.

[32] Z. Hong, T. Coombs, Numerical modelling of AC loss in coated conductors by finite element software using H formulation, Journal of Superconductivity and Novel Magnetism 23 (2010) 1551–1562.

[33] N. M. Strickland, C. Hoffmann, S. C. Wimbush, A 1 kA-class cryogen-free critical current characterization system for superconducting coated conductors, Review of Scientific Instruments 85 (2014) 113907.

[34] V. M. R. Zermeño, K. Habelok, M. Stępień, F. Grilli, A parameter-free method to extract the superconductor's $J_c(B, \theta)$ field-dependence from in-field current–voltage characteristics of high temperature superconductor tapes, Superconductor Science and Technology 30 (2017) 034001.

[35] M. D. Ainslie, C. W. Bumby, Z. Jiang, R. Toyomoto, N. Amemiya, Numerical modelling of dynamic resistance in high-temperature superconducting coated-conductor wires, Superconductor Science and Technology 31 (2018) 074003.

[36] K & J Magnetics, Inc. Temperature and Neodymium Magnets, https://www.kjmagnetics.com/blog.asp?p=temperature-and-neodymium-magnets, 2021. Accessed: 2021-10-20.

[37] E. Zeldov, J. R. Clem, M. McElfresh, M. Darwin, Magnetization and transport currents in thin superconducting films, Physical Review B 49 (1994) 9802–9822.

[38] Z. Jiang, R. Toyomoto, N. Amemiya, X. Zhang, C. W. Bumby, Dynamic resistance of a high-T_c coated conductor wire in a perpendicular magnetic field at 77 K, Superconductor Science and Technology 30 (2017) 03LT01.

[39] C. P. Bean, Magnetization of hard superconductors, Physical Review Letters 8 (1962) 250–253.

[40] C. P. Bean, Magnetization of high-field superconductors, Reviews of Modern Physics 36 (1964) 31–39.

[41] T. Woodcock, Y. Zhang, G. Hrkac, G. Ciuta, N. Dempsey, T. Schrefl, O. Gutfleisch, D. Givord, Understanding the microstructure and coercivity of high performance NdFeB-based magnets, Scripta Materialia 67 (2012) 536–541.

[42] SuperCurrent high-temperature superconducting wire critical current database, https://www.robinson.ac.nz/hts-wire-database, 2021. Accessed: 2021-10-20.